Enhancing railway network safety by reproducing wheel–rail electrical contact on a laboratory scale

Luna Haydar, Florent Loete, Frédéric Houzé, Tanguy Choupin, Fabien Guiche, Philippe Teste

applied sciences

MDPI

Article

Enhancing Railway Network Safety by Reproducing Wheel–Rail Electrical Contact on a Laboratory Scale

Luna Haydar [1,2], Florent Loete [2,*], Frédéric Houzé [2], Tanguy Choupin [1], Fabien Guiche [3] and Philippe Testé [2]

[1] SNCF, Direction Technologies Innovation et Projets Groupe, 1-3 Avenue François Mitterrand, 92300 La Plaine Saint Denis, France
[2] GeePs, Group of Electrical Engineering Paris, CNRS, CentraleSupélec, Université Paris-Saclay, 3 & 11 Rue Joliot-Curie, 91192 Gif-sur-Yvette, France
[3] SNCF Réseau, Direction Générale Industrielle & Ingénierie, Direction Technique Réseau, Département de la Signalisation Ferroviaire, 6 Avenue François Mitterrand, 93574 La Plaine Saint Denis, France
* Correspondence: florent.loete@centralesupelec.fr

Abstract: Ensuring the safety of rail networks requires precise detection of a train's position on a track section. This is achieved using a "track circuit" system, in which the wheel–rail electrical contact is the key to maintaining the system's reliability. However, any degradation of this contact can lead to a track circuit malfunction known as "deshunting", creating a serious safety risk for the rail network and for passengers. This paper presents a refined approach to this concern by implementing a laboratory-scale test bench. The main objective is to reproduce the wheel–rail electrical contact under controlled conditions to better understand the various aspects of this contact. The criteria governing the dimensioning of the test bench at reduced scale are based primarily on mechanical considerations. In this study, a series of tests were carried out to investigate the behavior of the electrical resistance as a function of various parameters such as load, current and time. An original homemade salt spray system was designed and used for obtaining controlled rail oxidation. Our preliminary results highlight the impact of these factors on the electrical resistance, providing valuable insights for future advances in rail safety technology.

Keywords: health monitoring; failure; deshunting; track circuit; wheel–rail electrical contact; oxidation; test bench

Citation: Haydar, L.; Loete, F.; Houzé, F.; Choupin, T.; Guiche, F.; Testé, P. Enhancing Railway Network Safety by Reproducing Wheel–Rail Electrical Contact on a Laboratory Scale. *Appl. Sci.* **2023**, *13*, 10253. https://doi.org/10.3390/app131810253

Academic Editor: José António Correia

Received: 1 August 2023
Revised: 26 August 2023
Accepted: 30 August 2023
Published: 13 September 2023

1. Introduction

The accurate localization of trains on railway tracks is crucial for ensuring the safety of railways. This is achieved through a technical device called the "track circuit", which provides real-time information about the presence of the train within a specific track section. When a train enters this zone, its wheels and axle create a short circuit between the two rails, indicating the occupancy of the zone. The signaling systems can be activated accordingly. Maintaining a high-quality wheel–rail contact is therefore a major issue for ensuring the reliability of the track circuit system and hence track safety. If this contact is affected by a third body of natural or artificial origin present in the interface, train detection can be jeopardized for a certain period, leading to the phenomenon known as "deshunting" where the train's presence is no longer detected. Despite the implementation of various devices to prevent [1] or reduce the occurrence of deshunting, many instances are still being detected every year.

The significant impact that deshunting events can have on railway management and on the occurrence of potentially dangerous situations, such as level crossing failures and rail accidents, has forced researchers to focus their attention on studying the behavior of the wheel–rail electrical contact interface. The wheel–rail contact is a very complex and multiphysical subject. In [2,3], the detection and impact of the mechanical deterioration of

the wheel rail was studied. The composition of the third body present at the wheel–rail interface may be complex, since it can include both external contaminants (dead leaves, frost, sand, oil...) and oxides formed naturally on surfaces [4]. Regarding oxides, composition was investigated using in situ X-ray diffraction. On the rail head, iron oxide, particularly in the form of FeOOH and Fe_3O_4, is the most dominant species [5]. Furthermore, Nakahara et al. provide a surface analysis by examining the concentration of oxide near the contact surface and the composition of both oxide and hydroxide [6]. In [7], the mechanical and electrical aspects of the third body (oxide layer) formed in the wheel–rail contact interface are examined through tribological, morphological and microscopic analyses. The study investigates the electrical conductivity, heterogeneity, continuity and compactness of the third body under both good and poor shunting conditions. Additionally, Fukuda et al. establish that several factors, including normal load, current intensity, oxide layer thickness and traffic frequency, can jointly influence the contact resistance [8]. A better understanding of wheel–rail electrical contact was also obtained through studies that were carried out on a 1/4 -scale test rig and on-site using an instrumented regional train [9,10]. These studies highlighted the non-linear $U - I$ characteristics, which are strongly dependent on the presence of oxide at the contact interface. These results show that scaled-down tests are in fact significantly representative compared to full-scale tests, demonstrating the relevance of performing such experiments. However, conducting tests at full-scale or even 1/4 -scale can be both cumbersome and costly, becoming an obstacle to rapid progress in this area of research.

The aim of this work is to develop a laboratory-scale rolling contact test bench that reduces the complexity and cost associated with conducting these experiments while faithfully reproducing wheel–rail electrical contact on a reduced scale. By analyzing various aspects of contact under reproducible conditions (controlled speed, load and oxidation state), we seek to improve our knowledge of the deshunting phenomenon. This paper focuses on the study of the influence of oxidation since it is one of the major causes of deshunting. The first performed tests to validate the bench consisted of investigating the resistance behavior in relation to different parameters such as load, current and time. Furthermore, the ease of developing controlled surface degradation protocols makes it easier to assess their impact on contact resistance. Overall, our work offers new perspectives and possibilities for improving railway systems.

2. Bench Conception

2.1. General Principle

The developed setup, presented in Figure 1, consists of a reduced-scale wheel running on a 1 m full-scale rail. An electrical actuator applies a normal force on the wheel axis inducing a pressure on the contact area equivalent to that produced by a real loaded train. The linear motion axis allows the wheel carriage to move along the rail at a controlled, scaled-down speed.

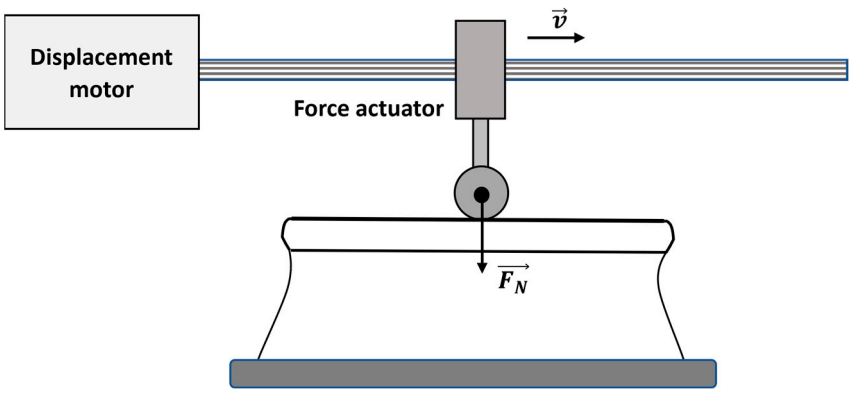

Figure 1. Schematic diagram of the test bench.

The bench was designed in order to be the most representative as possible of the devices most likely to be involved in deshunting problems. Electrically, the aim was to simulate the most extensively used track circuit on the French rail network (FRN).

The sizing of the reduced scale wheel (hereinafter referred to as the roller), the load applied and the speed of the displacement were estimated as explained in Section 2.2.

Our major concern was to reproduce the physical behavior of the contact interface. Consequently, we had to carefully study the impact of the downscaling on the dimensions of the setup.

2.2. Dimensioning Methodology

Mechanical laws were considered when scaling the test bench to be the most representative of the full-scale behavior of the wheel–rail contact.

The test bench was designed following three criteria:

1. Same aspect ratio of the contact surface at both scales.
2. Same average contact pressure at both scales.
3. Same fraction of contact surface renewed at both scales during a track circuit signal period.

2.2.1. Choice of the Roller

The shape of the roller was chosen to ensure that the contact surface between the wheel and the rail was geometrically similar at both scales. To estimate the wheel–rail contact surface, we relied on Hertz's theory, which is a widely-used reference, although we were aware that its assumptions would only be partially satisfied. Hertz's theory assumes:

- Perfectly elastic and homogeneous bodies in contact with isotropic mechanical properties.
- Smooth contact surfaces.
- Semi-infinite bodies with contact dimensions very small compared to body dimensions and radii of curvature.

According to Hertz's theory [11], the contact surface forms an ellipse. The surface and semi-axes (a, b) are given by the following expressions:

$$\begin{aligned} S_{contact} &= \pi * m * n * \left(\frac{3}{2} * F_N * \left(\frac{1-v^2}{E}\right) * \left(\frac{1}{A+B}\right)\right)^{\frac{2}{3}} \\ a &= m * \left(\frac{3}{2} * F_N * \left(\frac{1-v^2}{E}\right) * \left(\frac{1}{A+B}\right)\right)^{\frac{1}{3}} \\ b &= n * \left(\frac{3}{2} * F_N * \left(\frac{1-v^2}{E}\right) * \left(\frac{1}{A+B}\right)\right)^{\frac{1}{3}} \end{aligned} \quad (1)$$

E and v: Young's modulus and Poisson's ratio of the steel.
A and B: combined longitudinal and transverse curvatures.
m and n: tabulated coefficients dependent on A and B [12].

Consequently, the first criterion means maintaining the same a/b ratio between the long and short axes of the elliptical contact surface on both scales.

Equation (1) leads to:

$$\left(\frac{m}{n}\right)_{scale1} = \left(\frac{m}{n}\right)_{reduced\ scale} \quad (2)$$

It is important to note that at full scale, the wheel can be assimilated to a cylinder when it is in contact with the rail (Figure 2, top). Considering that the curvature radius of the head of the rail $R_{c\ rail}$ is unchanged and the scaling ratio of the wheel, the shape of the contact surface in the transverse direction would have been a rectangle.

To satisfy the first criterion, the rolling face of the wheel was chosen to be toroidal, as pictured in Figure 2, at the bottom.

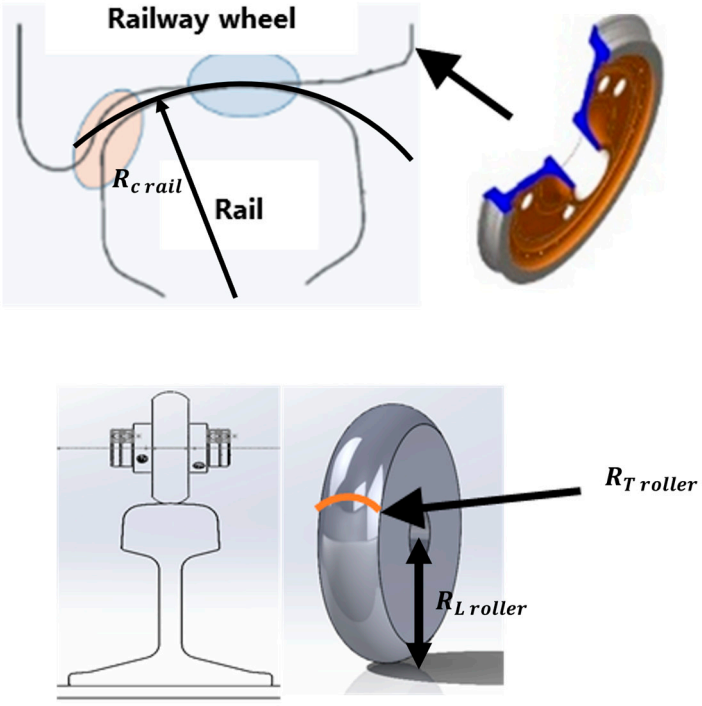

Figure 2. Wheel–rail contact at full scale (**top**) [13] and at reduced scale (**bottom**).

The transverse radius of curvature $R_{T\ roller}$ allows us to adjust the shape of the contact surface while maintaining the desired a/b ratio. Using Equation (2) and [12], the following relation can be derived:

$$R_{T\ roller} = \frac{1}{\frac{1}{R_{L\ roller}}\left(\frac{1+\left(\frac{m}{n}\right)_{scale1}}{1-\left(\frac{m}{n}\right)_{scale1}}\right) - \frac{1}{R_{T\ rail}}} \tag{3}$$

For design purposes, the final longitudinal radius $R_{L\ roller}$ value was 30 mm. This value allows for several full revolutions of the roller along the 1 m rail on the bench. The corresponding transverse radius $R_{T\ roller}$ = 15.4 mm allowing us to maintain the a/b *ratio* was determined using (3).

2.2.2. Choice of Force Actuator

According to the second criterion, the choice of the force actuator was made to maintain the same average contact pressure at both scales (denoted respectively as $P_{scale\ 1}$ and $P_{reduced\ scale}$):

$$P_{scale\ 1} = P_{reduced\ scale} \tag{4}$$

Knowing the normal forces per wheel of a full-scale train and its size, and using Hertz' Equation (1), we calculated the normal force to be applied at the reduced scale using the following equation:

$$F_{N\ reduced\ scale} = P_{scale\ 1} * S_{contact\ reduced\ scale} \tag{5}$$

An abacus was developed to determine the appropriate normal force required on the reduced scale for a given roller radius to maintain the same average pressure applied as at full scale. Considering the trains that are the most subject to deshunting, the full scale load per wheel ranges from 55 kN to 105 kN, resulting in a 235 N to 430 N range at reduced scale for a roller with $R_{L\ roller}$ = 30 mm and $R_{T\ roller}$ = 15.4 mm. Table 1 gives a comparison of the scaled parameters versus the real case resulting from the previous dimensioning.

Table 1. Comparison of the scaled contact with the real life one for the considered railcar and rail profile.

	Scale 1	**Reduced Scale**
R_L	420 mm	30 mm
R_T	∞	15.4 mm
Normal force	76.9 kN	392 N
Contact surface	85.1 mm^2	0.43 mm^2
a	6.6 mm	0.47 mm
b	4 mm	0.29 mm
Average pressure	903 MPa	903 MPa

2.2.3. Speed Scaling

Considering the third criterion, the speed v of the wheel carriage was chosen to maintain the same fraction of renewed contact area (denoted $A_{relative\ renewed\ contact}$) during a track circuit signal period Δt at both scales. The calculation of this relative area is developed in Appendix A. It is expressed as:

$$\begin{gathered} A_{relative\ renewed\ contact}(t_0+\Delta t) = 1 - \frac{2}{\pi}\mathrm{arc}tan\left(\frac{a}{b}\tan(\alpha)\right) + \frac{4S}{\pi ab} \\ \text{where} \quad \alpha = \arctan\left(\frac{2b\sqrt{1-\frac{v^2\Delta t^2}{4a^2}}}{v\Delta t}\right) \\ \text{and} \quad S = \frac{1}{2}v{\cdot}b{\cdot}\Delta t\sqrt{1-\frac{v^2\Delta t^2}{4a^2}} \end{gathered} \tag{6}$$

The extreme case of this criterion corresponds to the minimum displacement speed at which the contact ellipse will be completely renewed within a track circuit signal period Δt. In this case, the contact interface comprises a "new" oxide layer at each current alternation. The minimum speed required to obtain a fully renewed contact ellipse is denoted by v_{2a}. It can be calculated using the following equation:

$$v_{2a} = 2 * a * f_{cdv} \tag{7}$$

where f_{cdv} is the frequency of the track circuit considered in our study (2.3 kHz).

Considering the example shown in Table 1, one can find that $v_{2a\ scale1}$ = 30.56 m/s and $v_{2a\ reduced\ scale}$ = 2.31 m/s, illustrating a 13.2 factor on the speed. This result is very important and convenient since it allows us to work at a reduced speed on the bench while reproducing the conditions of higher real-life speeds.

2.3. Four-Point Electrical Measurements

The measurement of the wheel–rail electrical contact resistance was performed using the four-point method, as shown in Figure 3b, which illustrates the principle of this technique applied to the test bench. Figure 3a shows a photograph of the concrete implementation, where two copper thread brushes were used to inject current from a source into the contact, while two other brushes (placed closest to the contact) were used to measure the contact voltage. The current flowing through the contact was evaluated by measuring the voltage V_s across a well-known shunt resistance R_s.

2.4. Surfaces Preparation

2.4.1. Reference Surfaces

To approach the conditions required by Hertz's theory, where surfaces are assumed to be perfectly smooth, efforts were made to improve the roughness of both the wheel and rail surfaces. In order to obtain a smoother surface, the wheel was polished using different grades of polishing paper. An evaluation of the overall surface quality (surface

defects) was performed using binocular observation, as shown in Figure 4. Additionally, a profilometer was then employed to measure the surface roughness. Based on more than 30 measurements, we found that the average and peak-to-peak roughness values were $R_a = 0.4$ µm and $R_t = 4.5$ µm, respectively.

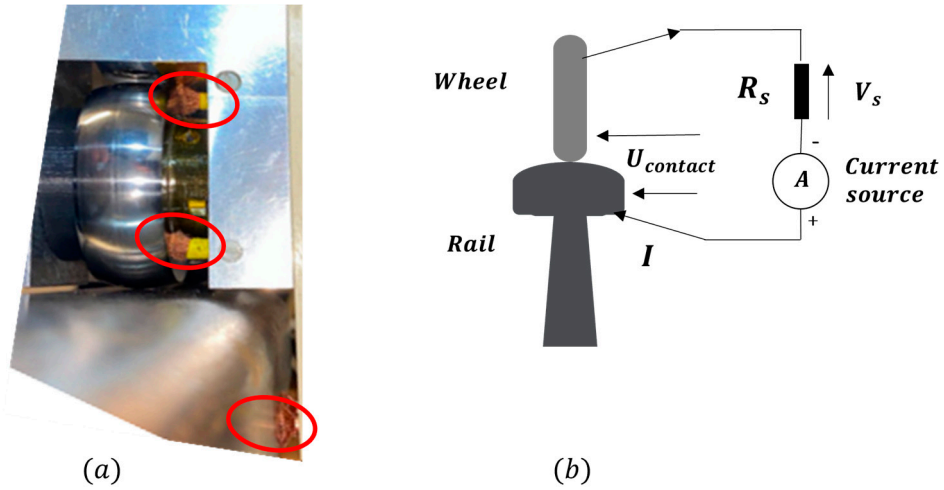

Figure 3. Electrical measurement system based on the four-point method: (**a**) photograph of the copper thread brushes (red circled), (**b**) schematic of the electrical measurement setup on the bench.

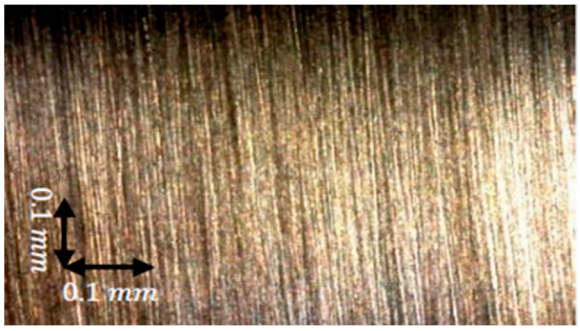

Figure 4. Improved wheel surface quality observed through a binocular lens.

As for the rail, the same polishing process was applied. However, given the complexity of assessing rail surface quality with binocular or profilometer observations, considering its size, a roughness tester from Mitutoyo ("SurfTest SJ301" model) was used. This device can evaluate arithmetic roughness (R_a) and other parameters associated with surface profile parameters. Based on more than 30 measurements within an arbitrary rail zone, the roughness values obtained were $R_a = 0.8$ µm for average roughness and $R_t = 8.2$ µm for peak-to-peak roughness.

Following this work, six distinct reference zones, shown in Figure 5, were delimited on the wheel where the visual aspect was observed and the roughness measured before and after the experiments, presented in Section 3.

2.4.2. Oxidation Protocol

To achieve severe, accelerated and controlled oxidation of the rails, we employed a homemade salt spray system. The principle of this system consists of spraying a saline solution with a NaCl concentration of 0.6 mol/L, similar to seawater, into a testing chamber, creating a favorable environment for oxidation. The saline solution is applied on the rail using misting nozzles and a watering programmer. The duration of misting and drying is adjusted according to the desired oxide thickness. After each oxidation process, the thickness of the oxide layer was measured using a probe from Fischer ("Deltascope FMP30"

model). This equipment operates on the principle of magnetic induction and is adapted to rough surfaces, with a precision of approximately ±0.2 µm for oxide thicknesses of up to 100 µm.

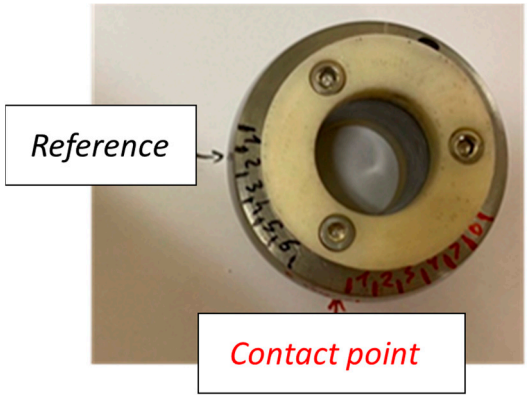

Figure 5. Six reference zones defined on the wheel after an improvement in polishing quality.

Figure 6 shows a preliminary oxidation performed on one rail using this system, resulting in severe oxidation and creating a case with a heavily oxidized zone showcasing an extreme example of an abandoned track. The average oxide thickness, based on more than 30 measurements, is 57 µm and has a standard deviation of 17 µm. This oxide thickness exceeds what is typically observed on low-traffic tracks, where oxide thickness varies from 1 to 2 µm on the rail tread and 5 to 6 µm on the peripheral zone. For the first try, the oxide thickness was intentionally exaggerated since it was difficult to evaluate its influence. Consequently, we aimed at realizing severe rust conditions to ensure deshunting occurrences.

Figure 6. Appearance of the rail compared to its initial state after a salt spray oxidation protocol.

3. Results

The tests presented in Sections 3.1–3.3 were carried out under static conditions (no rolling) and with direct current, using a Keithley 2400 sourcemeter in four-probe mode to inject current and measure contact resistance.

3.1. Dependence of the Resistance on the Applied Force

This section focuses on the effect of applied force on the contact resistance. In Hertz's theory, the contact resistance as a function of force is predicted to follow a power-law behavior $R_c \sim F^{-\frac{1}{3}}$.

The contact resistance was evaluated with a constant DC current of 0.1 A. The applied load was progressively increased from 30 N to 430 N (maximum force as explained in Section 2.2.2), then decreased to 30 N.

Initially the tests were conducted on three zones under normal conditions, in ambient air. In Figure 7, we present the $R_c - F$ characteristics obtained from one of these zones.

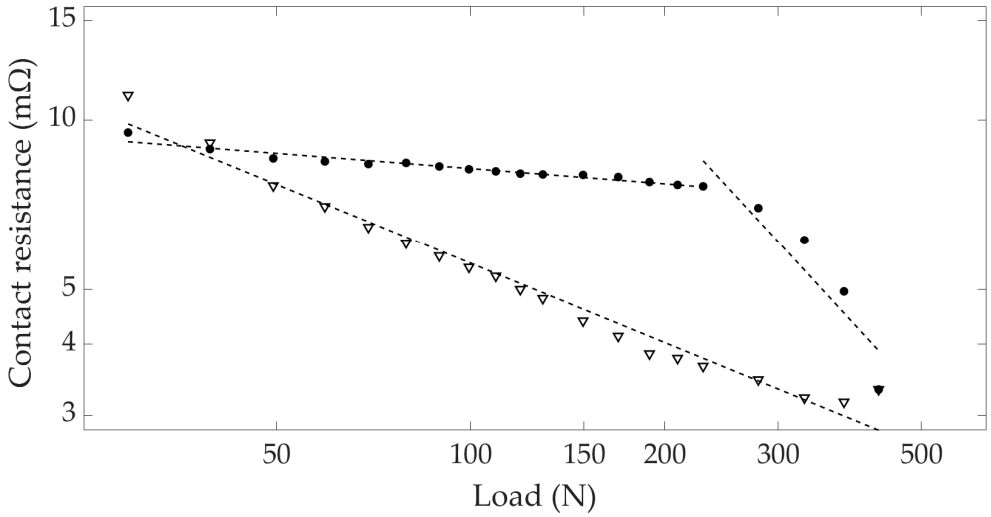

Figure 7. In air—$Log - logR_c - F$ characteristics at imposed DC current I = 0.1 A. Increasing the load (●) then decreasing it (▽). (--): experimental fits of the various sections.

These force tests conducted in ambient air reveal unexpected contact resistance behaviors far from those predicted by Hertz. At lower forces (<230 N), the resistance decreases very slowly, following a power-law $R_c \sim F^{-0.09}$. Beyond 230 N, the resistance exhibits a much more pronounced decrease, following a power-law $R_c \sim F^{-1.24}$ with an exponent greater than one. When decreasing the force from 430 N to 30 N the resistance follows a $R_c \sim F^{-0.47}$ power-law. These observations may reflect the extreme difficulty of obtaining perfectly smooth, clean surfaces on both wheel and rail. Surface roughness, contamination and possible oxidation make it impossible to achieve ideal Hertz's conditions.

To address these unexpected results and evaluate the potential impact of oxidation on the contact resistance, the test was replicated on three other zones using a nitrogen jet to create a controlled environment. In Figure 8, we present the $R_c - F$ characteristics obtained from one zone with nitrogen exposure. When increasing the force from 30 N to 230 N, the resistance closely follows a power-law $R_c \sim F^{-0.31}$, thus approaching the Hertzian law. This indicates that the application of the nitrogen jet effectively eliminated some external factors and thus allowed for approaching Hertz conditions in this force range. However, beyond 230 N, the resistance evolution again deviates as for the ambient air experiment, following a greater power-law, $R_c \sim F^{-2}$. When decreasing the force from 430 N to 30 N, the resistance follows a $R_c \sim F^{-0.76}$ power-law.

This change in resistance behavior for forces beyond 230 N can be attributed to the occurrence of permanent deformation (plasticity of asperities). A similar behavior was

observed in a previous study [14], which focused on a single electrical contact between two grains of copper powder subjected to a mechanical pressure P in the plastic regime. In this study, it was found that the resistance demonstrated a power-law dependence on the force, with an exponent greater than one. This peculiar behavior was attributed to the presence of microchannels at the contact area between the two grains, characterized by wide-ranging conductances.

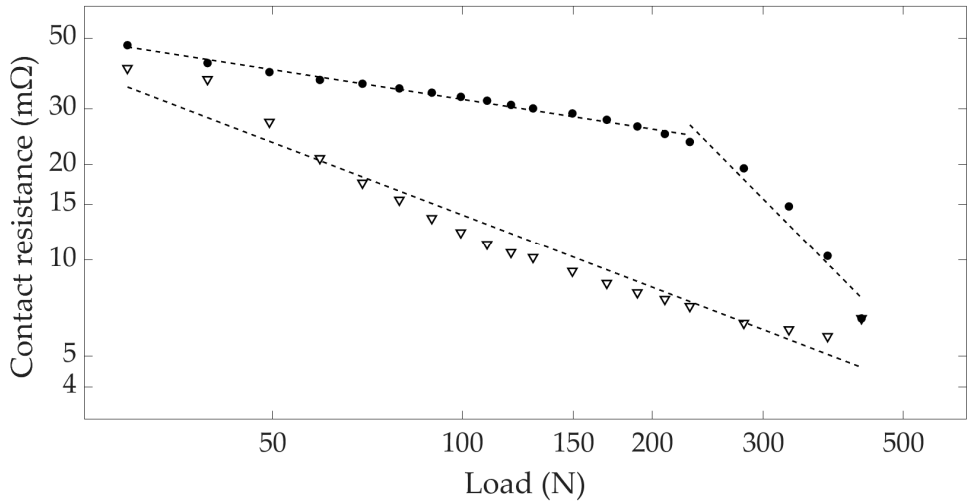

Figure 8. With a nitrogen jet—Log-log $R_c - F$ characteristics at imposed DC current $I = 0.1$ A. Increasing the load (•) then decreasing it (▽). (--): experimental fits of the various sections.

During the return phase (decreasing force), for both air and nitrogen conditions, the resistance follows a different path, which can be explained by the persistent asperity flattening [15].

3.2. Dependence of the Resistance on the Applied Current

The main objective of this experiment was to explore the impact of the applied current on contact resistance. To this end, contact resistance measurements were carried out on different areas of the rail under static conditions. Increasing and decreasing currents were applied, from 100 mA to 1 A and vice versa, with 100 mA steps every 60 s. The evolution of the applied current intensity is shown in Figure 9. The contact voltage was measured every second.

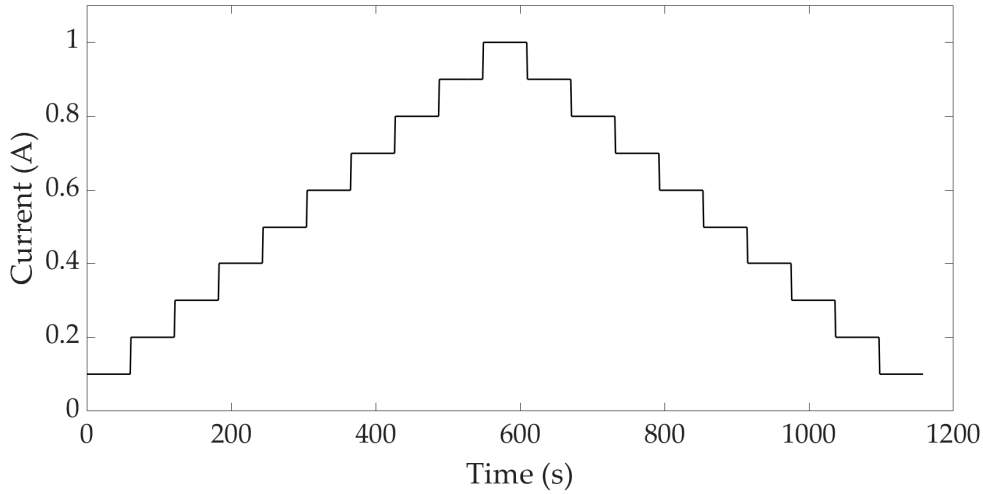

Figure 9. Current I (A) versus time t (s). The current was increased from 0.1 A to 1 A, then decreased from 1 A to 0.1 A by 0.1 A every 60 s.

These tests were conducted on both a clean and oxidized contact area (oxide thickness = 57 µm).

3.2.1. Clean Contact: $R_c(I)$

For a clean contact, Figure 10 shows the variation in current and voltage over time. The corresponding *U-I* characteristic is shown in Figure 11. It presents a linear-ohmic and reversible behavior. In this case, the increasing and decreasing *U-I* characteristics are perfectly superposable on each other. $R_c(I)$ was evaluated at 10 mΩ, which is consistent with a contact on bare metal.

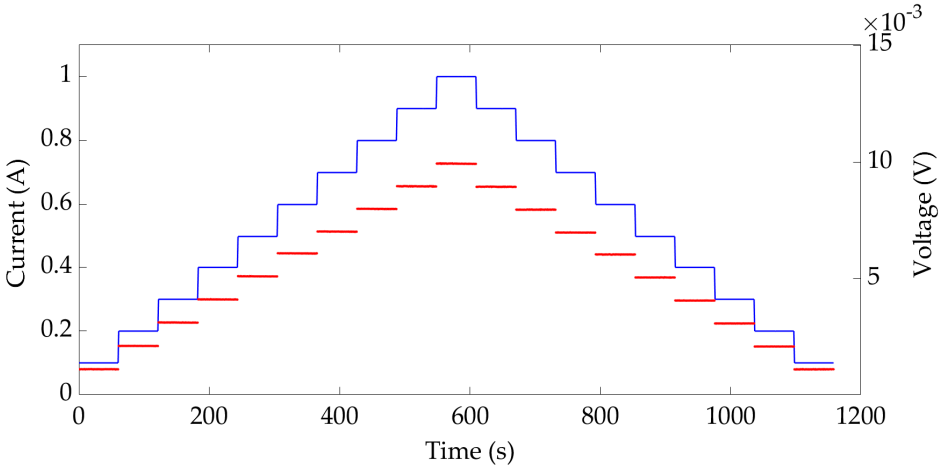

Figure 10. Evolution of the current intensity in the contact (—) and the contact voltage (—) over time for a clean contact between wheel and rail.

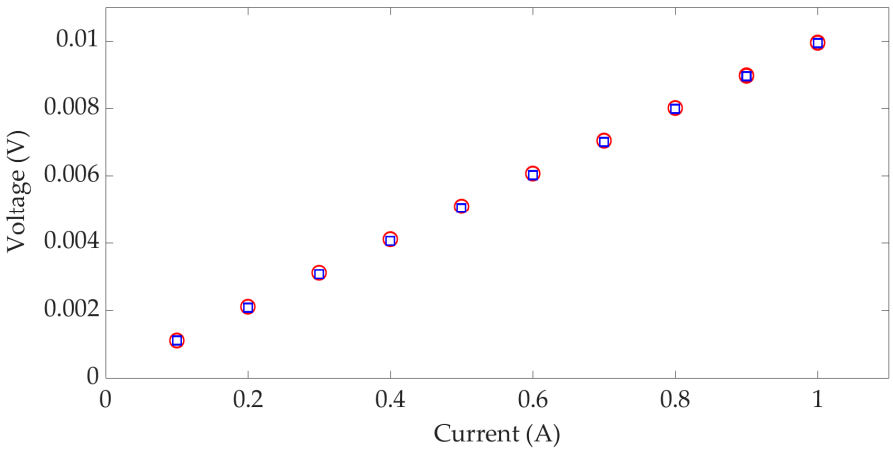

Figure 11. $U - I$ characteristics of a clean contact between wheel and rail when increasing the current I (○) from 0.1 A to 1 A, then decreasing I (□) from 1 A to 0.1 A, for F = 400 N.

3.2.2. Oxidized Contact: $R_c(I)$

Figure 12 shows the evolution of the current imposed on the contact (similar to the previous case) as a function of time, and the corresponding evolution of the contact voltage in the case of an oxidized surface. Figures 13 and 14 show the evolution of the contact resistance and the $U - I$ characteristics, respectively, during this experiment.

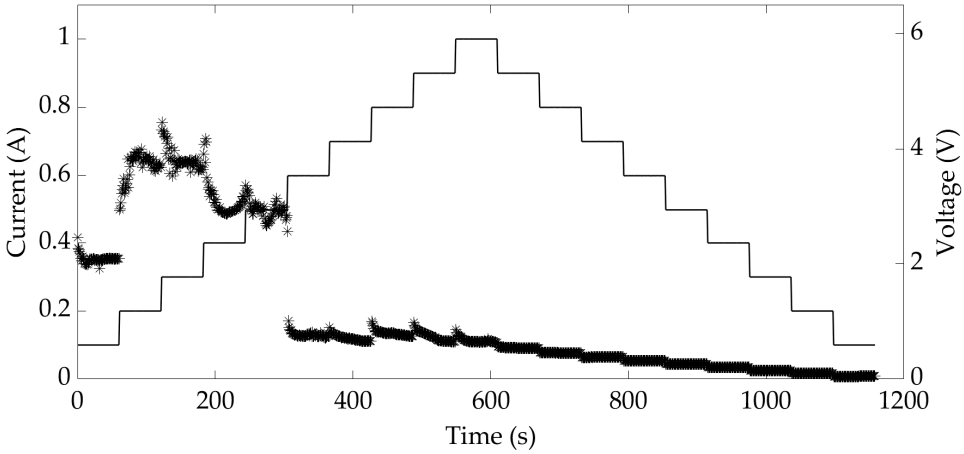

Figure 12. Evolution of the current intensity in the contact (− left axis) and the contact voltage (∗ right axis) over time for an oxidized contact.

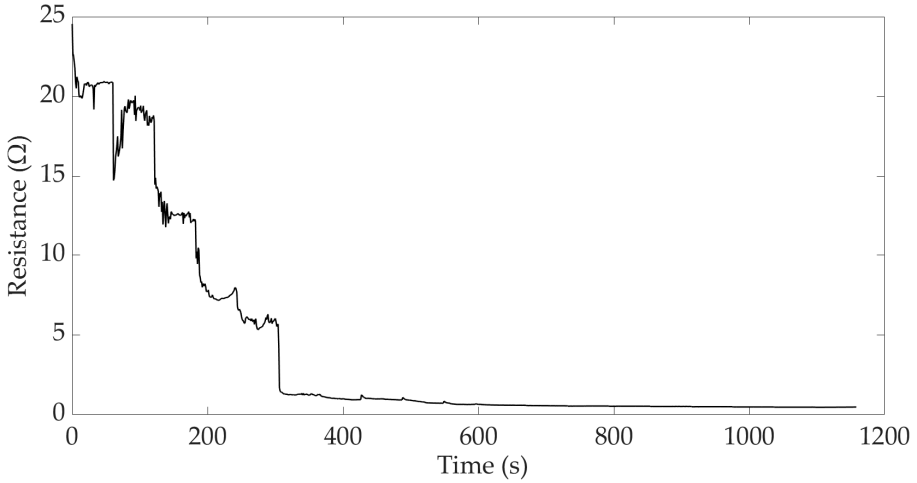

Figure 13. Evolution of the contact resistance over time for an oxidized contact, applying successive steps of increasing and then decreasing current.

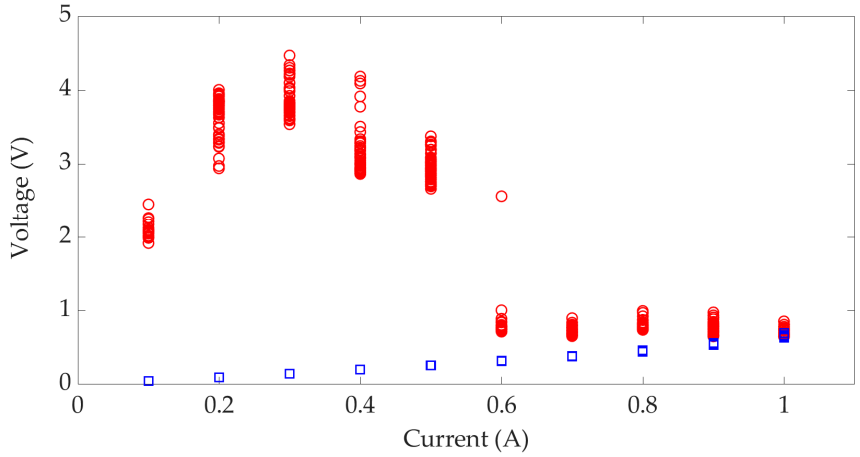

Figure 14. $U - I$ characteristics of an oxidized contact when increasing the current I (○) from 0.1 A to 1 A, then decreasing I (□) from 1 A to 0.1 A, for F = 400 N.

For an oxidized contact, the results reveal very different behavior compared to the one observed on the clean contact. Initially, as the current flows, a rapid evolution of the

contact occurs, observed as sudden drops in contact resistance with steps of increasing current. This can be observed at the beginning of the curves in Figures 12 and 13: up to 300 s and indicating a transition to a less insulating state. This behavior could be the result of an improved contact due to the flattening of surface asperities under the effect of mechanical stress and the heating generated by the current. As the current continues to increase, the contact resistance gradually stabilizes, indicating a slower evolution of the contact, as shown in Figure 14 after current increase from 0.6 A to 1 A. As the current decreases, $U - I$ characteristics become more linear, and the resistance tends to stabilize at a lower level (approximately 9.8 mΩ) than its previous values. This behavior is similar to that of a clean contact, as shown Figures 10 and 11, where the voltage is proportional to the current. Overall, the results indicate progressive changes in contact resistance, underlining the influence of current on the electrical properties of an oxidized contact.

3.3. Evolution of the Contact Resistance at Constant Current over a Long Period

The objective of this test was to observe the evolution of the contact resistance over time under static conditions while applying a constant current. To this end, we chose the maximum value of 1 A imposed during previous tests, the force applied to the contact always being 400 N.

To approximate a moderate rust condition, the oxide thickness on the rail was adjusted to around 20µm with a standard deviation of 5.9µm. Figure 15 shows the evolution of the contact resistance for a total current injection time of 80 min. The experimental approach consisted of four distinct phases:

- Phase 1: 1 A applied for 10 min. The current injection and the measurements were interrupted for a few minutes to see if the contact would return to its initial electrical state.
- Phase 2: 1 A applied for 40 min.
- Phase 3: 10 mA applied for 10 min.
- Phase 4: 1 A applied for 20 min.

During phase 1, a significant initial increase then decrease in resistance was observed, followed by a gradual decrease. After the interruption of the current, the resistance in phase 2 continued to decrease progressively starting from a contact resistance value close to the one reached at the end of phase 1. The third phase showed a slight increase in the contact resistance with an almost constant value. Finally, in phase 4, a gradual decrease in resistance was observed, reaching the same value as at the end of the second phase.

Considered jointly with the results presented in Section 3.2.2, the sudden drop in contact resistance at the beginning of the first phase may be interpreted as an irreversible change in the surface condition of the contact zone caused by mechanical and thermal effects. We assume that the start of phase 1 mainly reflects the melting of the peak asperities. Once flattened, the mechanical and thermal effects are spread over a wider and wider surface, which slows down the process. Thus, the progressive decrease of the contact resistance during the end of phase 1 and phases 2 and 4 could be explained by a slow continuation of the flattening of surface asperities, associated with an increase in oxide conductivity due to the rise in temperature (induced by the current). During phase 3, the current was decreased, resulting in a reduced heating effect. Therefore, the observed resistance increase could be interpreted as the presence of a semiconducting oxide layer at the interface.

3.4. Measurements during Rolling Contact on Rusted Rail

In this section, we present preliminary measurements on a wheel–rail rolling contact under a normal load of 400 N and an AC supply current with a frequency signal of 2.3 kHz and 0.1 A peak to peak. These parameters are based on an actual track circuit configuration used on the FRN, as explained in Section 2.1. The rail is the one rusted according to the protocol described above. The rolling contact was displaced at a constant speed of 1 cm/s.

Figure 16 illustrates the voltage drop across the wheel–rail contact and a known shunt resistance (the latter giving the image of the current). The voltage signal at the rusted

contact exhibits a series of transient state with elevated contact resistance, characterized by frequent peaks. The phases of high-resistance transients could in real life give rise to deshunting occurrences.

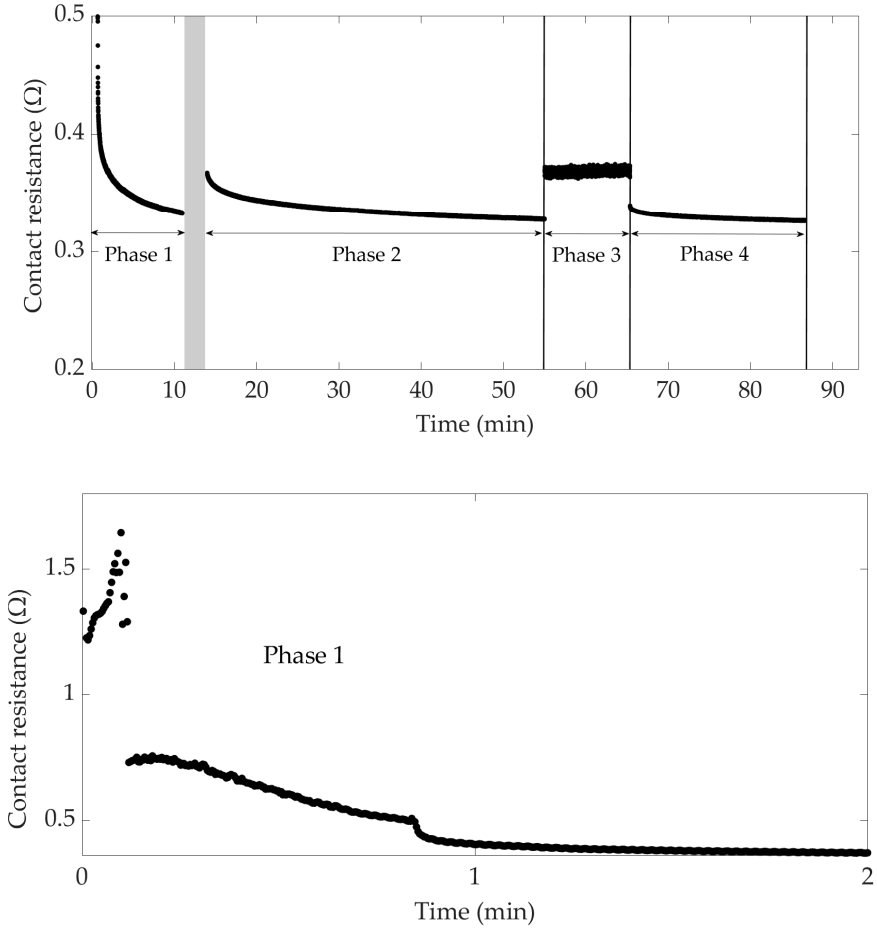

Figure 15. (**Top**) Evolution of the contact resistance of an oxidized wheel–rail contact during 4 phases: (Phase 1) injecting a current of 1 A for 10 min, (Phase 2) injecting a current of 1 A for 40 min, (Phase 3) injecting a current of 0.01 A for 10 min, (Phase 4) injecting a current of 1 A for 10 min. Between phase 1 and phase 2, current and measurement are interrupted during a few minutes (grey zone). (**Bottom**) zoom on phase 1.

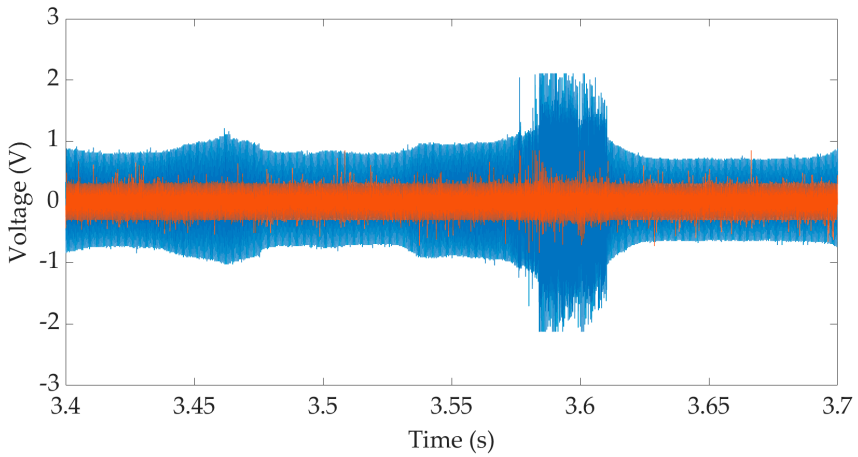

Figure 16. Voltage drop evolution across (—) the wheel–rail rolling contact and (—) a known shunt resistance (6.8 Ω) during rolling contact under 400 N normal load on rusted rail.

Figure 17 shows a closer examination of the voltage signals across the wheel–rail contact and the shunt resistance, revealing distinct behaviors. The left side of the figure presents a case of high contact resistance, resulting in significant signal deformation and non-linearity. Conversely, the right side of the figure corresponds to a healthier contact with lower resistance, where signals present more linear behavior.

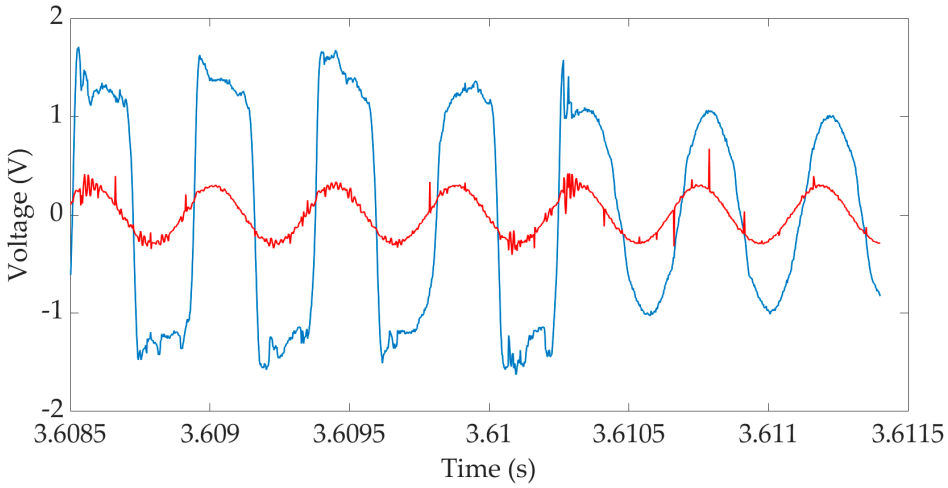

Figure 17. Detailed view over a few periods showing voltage drop evolution across (blue curve) the wheel-rail rolling contact and (red curve) a known shunt resistance (6.8 Ω) during rolling contact under 400 N normal load on rusted wheel–rail contact elements.

The high contact resistance and nonlinear behaviors of Figures 16 and 17 match the results previously observed in [10] with a 1/4 down-scaled test bench and a train on a real line. Consequently, the designed bench can be considered representative of the phenomenon at full scale.

To gain further insight into this complex phenomenon of rolling contact behavior, future studies are envisaged. These studies will continue to focus on understanding and characterizing rolling contact behavior as a function of various parameters such as current intensity, frequency, oxide thickness and displacement speed.

4. Conclusions

In this study, we designed a scaled-down rolling contact test bench that is able to mimic the wheel rail electrical contact of a train at the laboratory scale. The design was based on mechanical considerations, and the criteria applied on the test bench can effectively reproduce wheel–rail electrical contact. The bench was coupled with an original homemade salt spray system designed for obtaining controlled rail oxidation. Through a series of carefully controlled tests, including variations in load and oxidation state, we validated that the electrical behaviors observed were coherent with the observations from previous works. In a second trial, the behavior of the wheel–rail contact in static and rolling conditions was studied in order to better understand the deshunting phenomenon.

In static conditions, the influence of contact force and current intensity was successively investigated. With regard to force, contact loading-unloading tests were carried out with previously polished surfaces and a DC current of 0.1 A. The resistance vs. force curves, plotted in log scale, show different patterns for loading and unloading: as force increases, resistance first decreases slightly, then more markedly; on return, resistance increases with an intermediate slope. We assume that this behavior, which is in most cases far from the Hertzian contact model, reflects the influence of the surface roughness remaining after polishing (measured peak-peak values of around 4 µm on the roller and 8 µm on the rail), with plastic deformation of asperities occurring between 200 and 300 N. With regard to current intensity, we compared non-oxidized and oxidized rail surfaces for a given wheel state and a contact force of 400 N, with the current being increased and then decreased in

steps between 0.1 and 1 A. In the case of "clean contact", the *U(I)* characteristics are found to be linear and reversible. In the case of an "oxidized contact", the initial resistance is much higher, and the increase in current is accompanied by several sudden decreases in resistance, reflecting an irreversible evolution that we interpret as the flattening of asperities softened by heating due to high local current densities. Long-term observations of the evolution of contact resistance at 1 A current seem to corroborate this explanation. On return, as the current decreases, the *U(I)* characteristics are almost linear, with a much smaller slope (resistance). This set of results in static shows that the experimental bench we have built allows to study how wheel–rail contact resistance may be affected by mechanical, thermal, chemical or electrochemical phenomena.

In rolling conditions, the very first feasibility tests, carried out under real-life conditions except speed (slower), revealed alternating zones of shunting and deshunting, with different possible deformations of the contact voltage signal compared to the sinusoidal imposed current signal for the latter. Such behaviors were observed in previous studies both on a reduced-scale laboratory bench and in 1:1 railway tests.

For further study, we intend to deepen our investigations by focusing on dynamic and AC tests in order to reproduce a wider variety of real-life railway situations and explore more fully the influence of key parameters on the deshunting phenomenon.

Author Contributions: Conceptualization, F.L., F.H. and P.T.; methodology, L.H., F.L., F.H. and P.T.; software, L.H. and F.L.; validation, F.L., F.H. and P.T.; formal analysis, L.H., F.L., F.H. and P.T.; investigation, L.H., F.L., F.H. and P.T.; resources, T.C. and F.G.; data curation, L.H.; writing—original draft preparation, L.H., F.L., F.H. and P.T.; writing—review and editing, F.L., F.H., T.C., F.G. and P.T.; visualization, L.H., F.L., F.H., T.C., F.G. and P.T.; supervision, F.L., F.H., T.C., F.G. and P.T.; project administration, F.L., F.H., T.C., F.G. and P.T.; funding acquisition, F.L., F.H. and P.T. All authors have read and agreed to the published version of the manuscript.

Funding: The research was funded by the Société nationale des chemins de fer français (SNCF), the French national railway network.

Institutional Review Board Statement: Not applicable.

Informed Consent Statement: Not applicable.

Data Availability Statement: The data is unavailable due to privacy restrictions.

Conflicts of Interest: The authors declare no conflict of interest.

Appendix A

Appendix A.1. Area of an Elliptical Sector

Consider an ellipse with semi-axes (a, b) and let $d\alpha$ be an elementary sector of this ellipse (Figure A1). We define it by the equation:

$$\frac{x^2(\alpha)}{a^2} + \frac{y^2(\alpha)}{b^2} = 1$$
$$R^2\left(\frac{cos^2(\alpha)}{a^2} + \frac{sin^2(\alpha)}{b^2}\right) = 1$$

We approximate the area dA of the elliptical sector, defined by an angle dα, by considering it equivalent to the area of a circular sector with radius $R(\alpha)$, under the assumption that dα is small. Thus, $dA = \frac{1}{2}R(\alpha)^2 d\alpha$.

Then, we found that the area of an elliptical sector between angles α_1 and α_2 is:

$$A = \frac{1}{2}\int_{\alpha_2}^{\alpha_1} \frac{1}{\frac{cos^2(\alpha)}{a^2} + \frac{sin^2(\alpha)}{b^2}} d\alpha$$
$$A = \frac{1}{2}\int_{\alpha_2}^{\alpha_1} \frac{1}{\frac{cos^2(\alpha)}{a^2}\left(1 + \frac{a^2 tan^2(\alpha)}{b^2}\right)} d\alpha$$
$$A = \frac{1}{2}\int_{\alpha_2}^{\alpha_1} \frac{a^2}{cos^2(\alpha)} \cdot \frac{1}{1 + \left(\frac{a}{b} tan(\alpha)\right)^2} d\alpha$$

Let $u = \frac{a}{b}tan(\alpha)$ and $u' = \frac{a}{b}\frac{1}{cos^2(\alpha)}$:

$$A = \frac{1}{2}\int_{\alpha_2}^{\alpha_1} ab\frac{a}{b\,cos^2(\alpha)} \cdot \frac{1}{1+\left(\frac{a}{b}tan(\alpha)\right)^2} d\alpha$$

Which leads to:

$$A = \left[\frac{ab}{2}\text{arc}tan\left(\frac{a}{b}tan(\alpha)\right)\right]_{\alpha_2}^{\alpha_1}$$

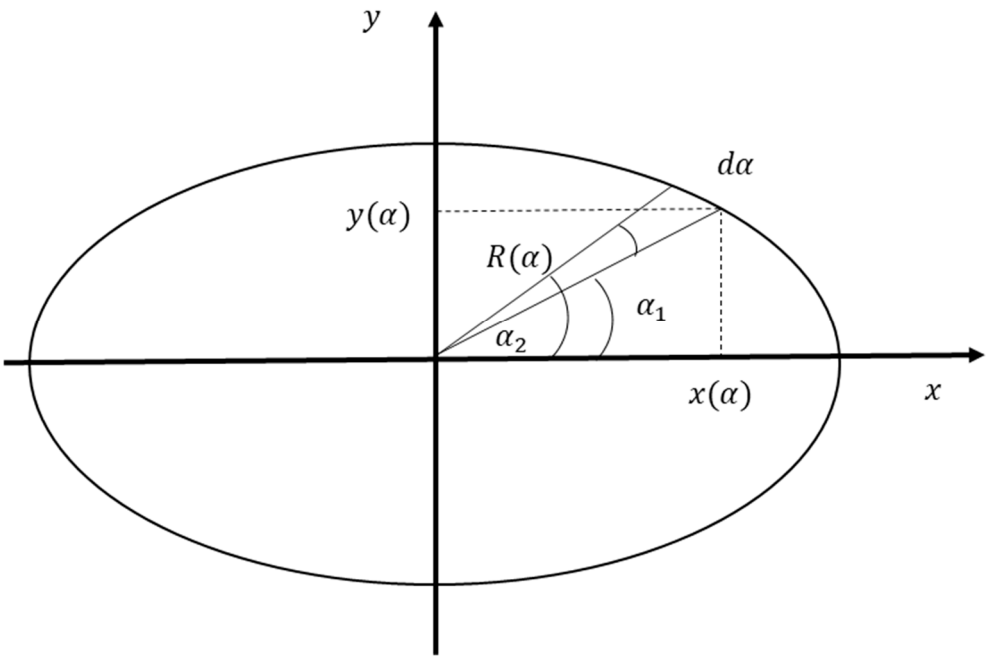

Figure A1. Elliptical surface with an elementary sector.

Appendix A.2. Calculation of $A_{relative\ renewed\ contact}$

Figure A2 illustrates the elliptical wheel–rail contact surface at instant t_0 and $t_0 + \Delta t$ when the train is running at speed v. Depending on v, there may be overlapping between these two ellipses. Let $A_{renewed\ contact}(t_0 + \Delta t)$ be the renewed contact surface during Δt.

The calculation of $A_{renewed\ contact}(t_0 + \Delta t)$ as a function of the displacement speed v is presented hereafter. Let O and O' be the centers of the two contact ellipses at instants t_0 and $t_0 + \Delta t$, respectively. Also, let M be the intersection point of these two ellipses.

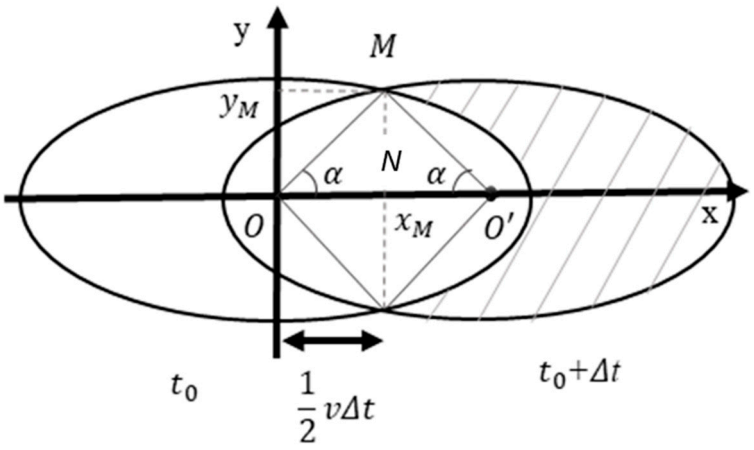

Figure A2. Renewed elliptical contact surface after a period of a track circuit period (Δt).

The area of the ONM triangle, denoted S, can be expressed as:

$$S = \frac{1}{2} \cdot x_M \cdot y_M$$

With:

$$\mathrm{M} \begin{cases} x_M = \frac{1}{2} v \Delta t \\ y_M = b\sqrt{1 - \frac{v^2 dt^2}{4a^2}} \end{cases}$$

Then:

$$\mathrm{S} = \frac{1}{2} v \cdot b \cdot \Delta t \sqrt{1 - \frac{v^2 \Delta t^2}{4a^2}}$$

Which leads to the expression of α, the angle between [ON] and [OM]:

$$\alpha = \arctan\left(\frac{2b\sqrt{1 - \frac{v^2 \Delta t^2}{4a^2}}}{v \Delta t}\right)$$

The renewed contact surface $A_{renewed\ contact}$ after a track circuit signal period Δt $(hatched\ surface)$ is:

$$\frac{1}{2} A_{renewed\ contact}(t_0 + \Delta t) = \frac{\pi ab}{4} + [A]_{\alpha}^{\frac{\pi}{2}} - \left([A_{renewed\ contact}]_0^{\alpha} - 2S\right)$$

Based on the calculation of the area of an elliptical sector in the Section 1 of the appendix:

$$A_{renewed\ contact}(t_0 + \Delta t) = \pi ab - 2ab \cdot \mathrm{arc}tan\left(\frac{a}{b}\tan(\alpha)\right) + 4S$$

And the relative renewed surface is given by:

$$A_{relative\ renewed\ contact}(t_0 + \Delta t) = \frac{A_{renewed\ contact}\ (t_0 + \Delta t)}{\pi ab}$$

Then:

$$A_{relative\ renewed\ contact}(t_0 + \Delta t) = 1 - \frac{2}{\pi}\mathrm{arc}tan\left(\frac{a}{b}\tan(\alpha)\right) + \frac{4S}{\pi ab}$$

References

1. Wybo, J.L. Track circuit reliability assessment for preventing railway accidents. *Saf. Sci.* **2018**, *110 Pt B*, 268–275. [CrossRef]
2. Mosleh, A.; Montenegro, P.A.; Costa, P.A.; Calçada, R. Railway Vehicle Wheel Flat Detection with Multiple Records Using Spectral Kurtosis Analysis. *Appl. Sci.* **2021**, *11*, 4002. [CrossRef]
3. Mosleh, A.; Montenegro, P.; Alves Costa, P.; Calçada, R. An approach for wheel flat detection of railway train wheels using envelope spectrum analysis. *Struct. Infrastruct. Eng.* **2021**, *17*, 1710–1729. [CrossRef]
4. Descartes, S.; Desrayaud, C.; Niccolini, E.; Berthier, Y. Presence and role of the third body in a wheel–rail contact. *Wear* **2005**, *258*, 1081–1090. [CrossRef]
5. Suzumura, J.; Sone, Y.; Ishizaki, A.; Yamashita, D.; Nakajima, Y.; Ishida, M. In situ X-ray analytical study on the alteration process of iron oxide layers at the railhead surface while under railway traffic. *Wear* **2011**, *271*, 47–53. [CrossRef]
6. Nakahara, T.; Baek, K.S.; Chen, H.; Ishida, M. Relationship between surface oxide layer and transient traction characteristics for two steel rollers under unlubricated and water lubricated conditions. In Proceedings of the 8th International Conference on Contact Mechanics and Wear of Rail/Wheel Systems (CM2009), Firenze, Italia, 15–18 September 2009.
7. Descartes, S.; Renouf, M.; Fillot, N.; Gautier, B.; Descamps, A.; Berthier, Y.; Demanche, P. A new mechanical-electrical approach to the wheel-rail contact. *Wear* **2008**, *265*, 1408–1416. [CrossRef]
8. Fukuda, M.; Terada, N.; Ban, T. Study of quantifying and reducing electrical resistance between wheels and rails. *Q. Rep. RTRI* **2008**, *49*, 158–162. [CrossRef]
9. Chollet, H.; Houzé, F.; Testé, P.; Loete, F.; Lorang, X.; Debucquoi, S. Observation of Branly's effect during shunting experiments on scaled wheel-rail contacts. In Proceedings of the 9th International Conference on Contact Mechanics and Wear of Rail/Wheel Systems (CM2012), Chengdu, China, 27–30 August 2012; pp. 111–114.

10. Houzé, F.; Chollet, H.; Testé, P.; Lorang, X.; Loëte, F.; Andlauer, R.; Debucquoi, S.; Lerdu, F.; Antoni, M. Electrical behaviour of the wheel-rail contact. In Proceedings of the 26th Inernational Conference on Electrical Contacts (ICEC-ICREPEC2012), Beijing, China, 14–17 May 2012; pp. 67–72.
11. Johnson, K.L. *Contact Mechanics*; Cambridge University Press: Cambridge, UK, 1985.
12. Toumi, M. Modélisation Numérique du Contact Roue-Rail pour l'Étude des Paramètres Influençant les Coefficients de Kalker: Application à la Dynamique Ferroviaire. Ph.D. Thesis, Université Paris-Est, Paris, France, 2016.
13. Nicodeme, C. Evaluation de l'Adhérence au Contact Roue-Rail par Analyse d'Images Spectrales. Ph.D. Thesis, Université Paris Sciences et Lettres, Paris, France, 2018.
14. Creyssels, M.; Falcon, E.; Castaing, B. Experiments and theory of the electrical conductivity of a compressed granular metal. *AIP Conf. Proc.* **2009**, *1145*, 123–126.
15. Timsit, R. Electrical Contact Resistance: Properties of Stationary Interfaces. *IEEE Trans. Compon. Packag. Technol.* **1999**, *22*, 1–19. [CrossRef]